

Matrix Stiffness Induces Epithelial-to-Mesenchymal Transition Via Piezo1-Regulated Calcium Flux

By

María López Cavestany

Thesis

Submitted to the Faculty of the
Graduate School of Vanderbilt University

In partial fulfillment of the requirements

For the degree of

MASTER OF SCIENCE

in

Biomedical Engineering

May 13th, 2022

Nashville, Tennessee

Approved:

Dr. Michael R. King

Dr. Cynthia A. Reinhart-King

This thesis is adapted from the following manuscript submitted for publication in the Journal of Cell Science:

“Matrix Stiffness Induces Epithelial-to-Mesenchymal Transition Via Piezo1-Regulated Calcium Flux in Prostate Cancer Cells”

Maria Lopez-Cavestany¹, Su Bin Hahn¹, Jacob M. Hope¹, Samantha C. Schwager¹, Joshua D. Greenlee¹, Jacob A. VanderBurgh¹, Cynthia A. Reinhart-King¹, Michael R. King^{1,*}

¹Department of Biomedical Engineering, Vanderbilt University, Nashville, TN, USA

*Corresponding author: mike.king@vanderbilt.edu

Acknowledgements

PA gel crosslinker application for PA gel collagen coating was conducted at the Vanderbilt Institute of Nanoscale Science and Engineering. This work was supported by the National Institute of Health National Cancer Institute grant number CA203991.

Table of Contents

Acknowledgements	iii
List of Figures.....	v
List of Abbreviations, Nomenclature, and Symbols	vi
Chapter 1: Introduction.....	1
Chapter 2: Materials & Methods.....	5
2.1 Cell Culture and Reagents	5
2.2 Polyacrylamide Gel Preparation.....	6
2.3 Calcium Imaging	8
2.4 Cell Shape and Actin Polymerization Assay	9
2.5 Western Blotting.....	11
Chapter 3: Results.....	13
3.1 Stiffer Substrates Lead to Increased Calcium Flux and Vimentin Expression.....	13
3.2 EMT Associated Characteristics Change with Stiffness	15
3.3 Calcium Flux Depends on Treatment and Stiffness	17
3.4 Effect of Yoda1 and GsMTx-4 on Vimentin Expression	22
3.5 Effect of Yoda1 and GsMTx-4 on EMT Morphology.....	25
Chapter 4: Discussion	32
Conclusion	37
References.....	38

List of Figures

Figure		Page
1	Summary of the effects of matrix stiffness on EMT progression in prostate cancer cells.....	3
2	Effect of stiffness on intracellular calcium concentration and vimentin expression.....	14
3	Effect of stiffness on EMT morphology in both PC3 and DU145 prostate cancer cells.....	16
4	Effects of pharmacological activation and inhibition on intracellular calcium concentration in PC3 cells at different stiffnesses.....	18
5	Effects of pharmacological activation and inhibition on intracellular calcium concentration at different stiffnesses in DU145 cells.....	21
6	Western blots showing the effects of pharmacological activation and inhibition of Piezo1 on substrates of increasing stiffness on total vimentin expression in PC3 and DU145 cells.....	23
7	Changes in PC3 aspect ratio and F-actin fluorescence with stiffness and pharmacological activation and inhibition of Piezo1.....	27
8	Effects of Yoda 1 and GsMTx-4 treatment on the aspect ratio and F-actin fluorescence of DU145 cells incubated on substrates of increasing stiffness.....	29

List of Abbreviations, Nomenclature, and Symbols

PA	Polyacrylamide
EMT	Epithelial-to-mesenchymal transition
F-Actin	Filamentous actin
AFM	Atomic force microscopy
ROI	Region of interest
SD	Standard deviation
BSA	Bovine serum albumin
$\Delta F/F_0$	Measurement of calcium flux

Chapter 1: Introduction

Epithelial-to-mesenchymal transition (EMT) has been associated with tumor progression and cancer metastasis, enabling cells to escape the primary tumor and extravasate into the bloodstream (Jolly et al., 2017). It is a combination of morphological and biochemical changes that reduce cell-cell recognition and adhesion leading to increased motility, invasiveness, and resistance to apoptosis (Heerboth et al., 2015; Kalluri and Weinberg, 2009). EMT is defined by changes in basement membrane remodeling, activation of differentiation genes, remodeling of the cytoskeleton, downregulation of epithelial proteins that aid in cell-to-cell adhesion (E-cadherin), and the upregulation of mesenchymal proteins such as N-cadherin and vimentin (Heerboth et al., 2015; Jolly et al., 2017; Roche, 2018). EMT is characterized by the acquisition of a mesenchymal cell morphology due to a loss of the apical-basal polarity of epithelial cells. However, EMT does not produce a stable cell state; it is a multi-dimensional process typically resulting in hybrid cells that fall between epithelial and mesenchymal states (Jolly et al., 2017; Roche, 2018).

There exists a complex array of signals which induce EMT, making it a highly heterogeneous process. These range from biochemical signals, interactions with other cell types such as stromal cells, and changes to the extracellular matrix (Emon et al., 2018). Increased extracellular matrix stiffness is known to play a prominent role in EMT and cancer metastasis (Bauer et al., 2020; Chen et al., 2021; Schrader et al., 2011; Wullkopf et al., 2018). In prostate cancer, the mean tumor stiffness is 60kPa as measured with transrectal shear-wave elastography, and ranges from 30kPa to 110kPa (Barr et al.,

2012). Moreover, there is a high degree of intratumoral stiffness heterogeneity (Ji et al., 2019; Rouvière et al., 2017). In contrast, healthy prostatic tissue has a maximum stiffness that ranges up to 35kPa (Correas et al., 2015).

As cells migrate through their environment, they exert tensile forces on the substrates (Janmey et al., 2019). This is counteracted by the viscoelastic properties of their surroundings as the matrix resists deformation. Cancer cells can sense these forces via mechanosensitive ion channels, which convert mechanical cues in the cells' environments to intracellular biochemical signals (**Fig. 1**). Piezo1, discovered by the 2021 Nobel prize winner for Physiology or Medicine Dr. Patapoutian, is a mechanosensitive ion channel that regulates calcium flux into cells by opening in direct response to lateral membrane tension and cytoskeletal tethers (Coste et al., 2012, 2010; Dombroski et al., 2021; Lin et al., 2019). In the closed/low tension state, Piezo1 stores potential energy for gating through its dome-like structure. When transitioning to the open state, the dome is flattened in proportion to the energy of the system. In this way, Piezo1 channels are gated by changing tension in the cell membrane with high sensitivity, resulting in increased calcium influx.

Under healthy conditions, Piezo1 allows endothelial cells to sense and react to shear forces in the bloodstream which helps to control vascular tone and the baroreceptor reflex (Fang et al., 2021). Additionally, Piezo1 plays a crucial role in the gastrointestinal tract, urinary tract, joints, lungs, and touch sensation. In prostate cancer, Piezo1 is highly upregulated compared to healthy prostatic tissue (Han et al., 2019).

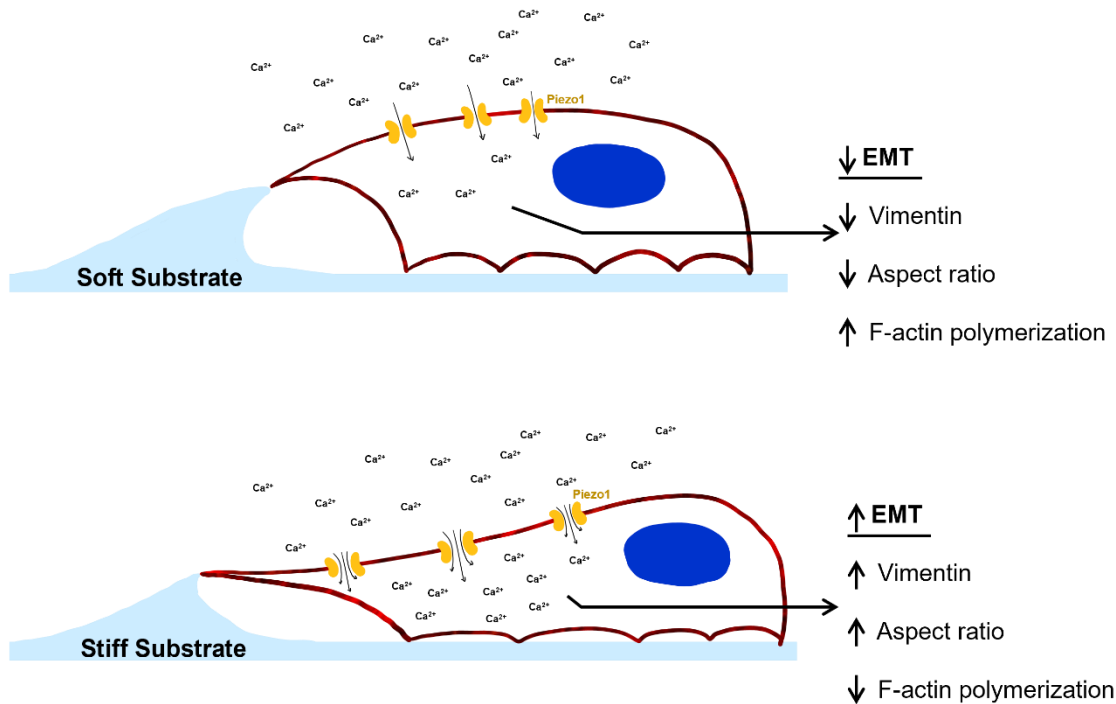


Figure 1. Summary of the effects of matrix stiffness on EMT progression in prostate cancer cells. Cells can modulate calcium flux into the intracellular space via mechanosensitive ion channels in the membrane, such as Piezo1. Piezo1 is opened by tension in the cell membrane as the matrix resists deformation when a cell pulls on it to migrate. This study connects how increasing matrix stiffness due to disease progression activates Piezo1, increases calcium influx, and leads to EMT in the prostate cancer cell lines PC3 and DU145.

This was observed in comparing para-carcinoma and carcinoma tissue samples isolated from a patient, and by comparing the prostate cancer cell lines PC3 and DU145 to the healthy prostate cell line RWPE-1. That study also found that Piezo1 plays a role in colony formation, cell migration, and wound healing *in vitro*. *In vivo*, Piezo1 silencing in

a murine subcutaneous model of prostate cancer led to decreased tumor volume and weight in the same study. Overall, evidence shows that Piezo1 is a key player in promoting cancer progression. In a separate study on prostate cancer, we showed that pharmacologically activating Piezo1 sensitized cells to TRAIL-mediated apoptosis in similar manner to that observed under the conditions of fluid shear stress (Hope et al., 2019). This further supports the importance of Piezo1 in various mechanisms of prostate cancer progression.

The current study expands on the understanding of how EMT is controlled via Piezo1 sensing of extracellular matrix stiffness surrounding cancerous cells. Herein, we model the biophysical environment of healthy and cancerous prostate tissue using polyacrylamide (PA) gels of different stiffnesses coated with collagen I. We then report on the effects of matrix stiffness and the pharmacological inactivation and activation of Piezo1 on EMT-associated changes in the metastatic prostate cancer cell lines PC3 and DU145. Significant changes in calcium influx, vimentin expression, and actin polymerization were observed in the high stiffness groups compared to cells on the low stiffness substrates. Additionally, these changes were comparable to those observed when both cell lines were grown on soft substrates while being treated with Yoda1, a chemical agonist of Piezo1.

Chapter 2: Materials & Methods

2.1 Cell Culture and Reagents

The metastatic prostate cell lines PC3 (CRL-1435, ATCC, Manassas, VA, USA) and DU145 (HTB-81, ATCC, Manassas, VA, USA) were cultured in RPMI 1640 media 1x (11875-093, Gibco, Paisley, UK) supplemented with 10% (v/v) fetal bovine serum (16140071, Gibco, Paisley, UK) and 1% (v/v) PenStrep (15140-122-100ML, Gibco, Grand Island, NY, USA). Cells were incubated in humidified conditions at 37°C and 5% CO₂ and passaged before exceeding 90% confluency. All experiments were performed in 6-well plates and substrates were sterilized under UV light for 45 min prior to cell seeding. Cells were washed in Ca²⁺ and Mg²⁺ free DPBS (21-031-CM, Corning, Manassas, VA, USA), treated with 0.05% trypsin-EDTA 1x (25300-054, Gibco, Grand Island, NY, USA) for 3 to 5 min, and resuspended in supplemented media before centrifugation at 300 x *g* for 5 min. Cell pellets were resuspended in supplemented media at a concentration of 0.2 x 10⁶ cells/mL, and 1mL of the cell suspension was pipetted into each well. Cells were incubated for a total of 72 hr on the substrates. To study the effect of pharmacologically activating Piezo1, cells were treated with 10µM Yoda1 (5586, Tocris, Minneapolis, MN, USA), and 0.1% (v/v) DMSO (4-X-5, ATCC, Manassas, VA, USA) was used as a vehicle control (Hope et al., 2019). To study the effect of pharmacologically inhibiting Piezo1, cells were treated with 2.5µM GsMTx-4 (ab141871, Abcam, Waltham, MA, USA), and 1.25% (v/v) DPBS with Ca²⁺ and Mg²⁺ (D1283-500ML, Sigma Life Science, St. Louis, MO,

USA) was used as a vehicle control. Treatments took place at the 24-hr mark during the 72-hr incubation, allowing cells time to adhere to the substrate surface prior to treatment.

2.2 Polyacrylamide Gel Preparation

22x22mm glass coverslips (1401-10, Globe Scientific, Mahwah, NJ, USA) were plasma cleaned with a PDC-001 plasma cleaner (Harrick Plasma, Ithaca, NY, USA) for 2 min and placed in a bath of 1% (v/v) polyethyleneimine (910791, Sigma Aldrich, St. Louis, MO, USA) in Milli-Q filtered water for 10 min. Coverslips were then washed 3 times in Milli-Q filtered water for 5 min and inverted onto a 200 μ L drop of a 0.1% (v/v) glutaraldehyde (G7776-10ML, Sigma Aldrich, St. Louis, MO, USA) in DPBS with Ca^{2+} and Mg^{2+} for 30 min. The coverslips were washed 3 additional times in Milli-Q filtered water for 5 min and dried overnight. PA gels with Young's modulus of 5kPa and 60kPa were synthesized by varying the concentrations of acrylamide solution relative to bis-acrylamide (Denisin and Pruitt, 2016). Gel precursor solutions were mixed for the 5kPa gel at a ratio of 7.5% (v/v) acrylamide solution (1610140, BOI RAD, Hercules, CA, USA) to 0.175% (v/v) bis-acrylamide solution (1610142, BIO RAD, Hercules, CA, USA), (Califano and Reinhart-King, 2008). The 60kPa gel precursor solution was prepared with a ratio of 13.5% (v/v) acrylamide solution to 0.42% (v/v) bis-acrylamide solution. Both precursor solutions also contained 0.05% (v/v) TEMED (T18000-0.25, Research Products International, Mt. Prospect, IL, USA) and 30mM HEPES (H4034-100G, Sigma Aldrich, St. Louis, MO, USA) pH=6, and were adjusted to pH=6. Solutions were degassed for 30 min and then polymerization was initiated by adding 10% (w/v) ammonium

persulfate (1610700, BIO RAD, Hercules, CA, USA) in Milli-Q filtered water, to reach a final concentration of 0.1% (w/v) of ammonium persulfate. A 40 μ L drop of the precursor solution was pipetted onto the activated side of the coverslip and sandwiched with a second 22x22mm coverslip coated in an anti-adherence solution for 1 hr. PA gels were then separated from the second cover slip and washed 3 times in PBS with Ca²⁺ and Mg²⁺.

For collagen coating, each gel was inverted onto a 100 μ L drop of 10mg/mL Sulfo-SANPAH (803332-50MG, Sigma Aldrich, St. Louis, MO, USA) in Milli-Q filtered water and cured using a UV flood exposure on a Karl Suss MA6 mask aligner in the Vanderbilt Institute for Nanoscale Science and Engineering (VINSE) cleanroom (Syed et al., 2015). After 3 washes in Milli-Q filtered water, gels were incubated on a 400 μ L drop of 0.1mg/mL collagen I (354236, Corning, Bedford, MA, USA) in HEPES pH=8 on ice for 2 hr. Finally, gels were incubated in 1mL of 1:1000 ethanolamine in PBS with Ca²⁺ and Mg²⁺ for 20 min. Glass coverslips without PA gels adhered to the surface were used as a positive control, simulating an extremely stiff environment for the cells. These surfaces were activated and then coated with collagen I following the procedure described above.

The PA gel elastic modulus was confirmed via contact mode atomic force microscopy (AFM) (MFP-3D Asylum Research, CA, USA) (Taufalele et al., 2019). Measurements were taken at 16 locations in each gel within a 120x120 μ m grid. Indentations were performed using a silicon nitride cantilever with a theoretical spring constant of 0.06N/m that had a borosilicate bead of 5 μ m in diameter attached at the tip (Novascan, Boone, IA). Before taking measurements, the AFM tips were calibrated, and the experimental spring constant was measured to be 0.163N/m \pm 0.019N/m. Asylum curve fitting software

was used to calculate the gel elastic modulus from the force curves using the Hertz model with a Poisson's ratio of 0.45 (**Fig. 2A**).

2.3 Calcium Imaging

To study the changes in calcium flux, the cellular probe Fluo-4 (F14201, Thermo Fischer Scientific, Milton Park, UK) was used. A stock solution of 50µg of Fluo-4 (F14201, Thermo Fischer Scientific, Milton Park, UK) in 50µL of pluronics (AS-84041, Anaspec Inc, Fremont, CA, USA) was prepared, and then was diluted down to 2µg/mL in serum-free RPMI 1640 (SFM). Substrates with cells grown for 3 days were transferred to clean 6-well plates with 1mL of Fluo-4 in SFM supplemented with each treatment: 10µM Yoda1, 0.1% (v/v) DMSO, 2.5µM GsMTx-4, and 1.25% (v/v) DPBS with Ca²⁺ and Mg²⁺. Cells were incubated in the dark at RT for 45 min and then washed with supplemented with each of the different treatments. Imaging was done on an Olympus IX81 inverted microscope using a 10x objective and a 510/20 (excitation/emission) filter set. Yoda1-treated cells grown on glass slides were imaged first to set the acquisition parameters. Images were taken at 5 random locations per substrate.

Image processing and analysis were performed with FIJI using the macro function and calculated using Eqn. 1. The first step was to identify the cells as regions of interest for mean fluorescence intensity measurement. All images were converted to 8-bit and then made binary via the thresholding tool. The thresholding parameters were set using an image from the Yoda1-treated cells grown on glass. Regions of interest (ROIs) were identified using the particle analyzer tool set to recognize features of 20 to 750µm² and

stored on the ROI manager. The original image was then reopened, the ROIs overlaid, and the mean fluorescence intensity was measured for each cell.

$$\frac{\Delta F}{F_0} = \frac{F_{average} - F_0}{F_0} \quad (1)$$

$F_{average}$ is the average of the mean fluorescence of all the cells for each of the 5 images taken. F_0 is the average fluorescent intensity of the background. This was sampled using the square tool on FIJI in 3 random locations and then averaged for each image. A total of 3 biological replicates were performed and the $\Delta F/F_0$ values for each of the 5 images for each were averaged and graphed on GraphPad Prism version 9 for Windows (GraphPad Software, San Diego, California USA). Unpaired, parametric t-tests were calculated using Prism and $p < 0.05$ was considered statistically significant. All values are presented as mean \pm standard deviation (SD). Images were pseudo-colored with the mpl-magma LUT on FIJI.

2.4 Cell Shape and Actin Polymerization Assay

Cells were fixed in 4% (v/v) paraformaldehyde (15714S, Electron Microscopy Sciences, Hatfield, PA, USA) in DPBS for 15 min, and then permeabilized in 1% (v/v) Triton-X-100 (9002-93-1, Sigma Aldrich, Darmstadt, Germany) in DPBS for 10 min. Blocking was done for 2 hr in 5% (v/v) bovine serum albumin (BSA) (A1470-100G, Sigma Aldrich, St. Louis, MO, USA) in DPBS and then the cells were stained with an ActinRed™ 555 ReadyProbes™ reagent (R37112, Invitrogen, Eugene, OR, USA) and 1.5:1000 DAPI (D1306, Invitrogen, Eugene, OR, USA) cocktail in 5% (v/v) BSA in DPBS. Coverslips with

a drop of antifade mounting media (H-1000, Vectrashield, Burlingame, CA, USA) were mounted onto glass slides (48311-703, VWR, Radnor, PA, USA).

Imaging was performed on an Olympus IX81 inverted microscope using a 20x objective. F-actin was observed using a 605/70 (excitation/emission) filter set and DAPI with a 460/50 (excitation/emission) filter set. 5 images of each treatment condition were captured at random locations around each substrate. A total of 3 biological replicates were performed for each of the treatments on the 3 different substrates. Image processing and analysis was performed on FIJI using the macro function. 10 random nuclei were selected for each image on the blue channel image. The blue channel (DAPI) and red channel (F-actin) were merged into composite images and then the 10 randomly selected cells were manually contoured using the freehand selections tool. ROIs were saved onto the ROI manager on FIJI. Aspect ratio and mean fluorescence were measured for all 10 contoured cells per condition. For F-actin fluorescence, background noise was sampled as described earlier for the calcium image analysis. **Eqn. 1** was used to calculate the $\Delta F/F_0$ value for each cell, where $F_{average}$ is each individual cell's mean fluorescence and F_0 represents the average of the 3 background measurements. All measurements were taken using the FIJI ROI manager measurement tool. Outliers were identified on GraphPad PRISM using a ROUT's test with Q set to 2% and removed from analysis. Data sets were graphed on Prism GraphPad and compared using an unpaired, parametric t-test, where $p < 0.05$ was considered statistically significant. All values are presented as mean \pm SD.

2.5 Western Blotting

Cells on substrates were rinsed with DPBS and lysed using 4x Laemmli sample buffer (1610747, BIO RAD, Hercules, CA, USA) supplemented with c0mplete tablets MINI, EDTA free protease inhibitor cocktail (4693159001, Sigma Aldrich, St. Louis, MO, USA). Electrophoresis using 10% sodium dodecyl sulfate-polyacrylamide gels was performed, followed by an overnight wet transfer onto a PVDF membrane (LC2002, Novex, Carlsbad, CA, USA) (Gallagher, 2007). The materials used for this were: 2-mercaptoethanol (M3148-100ML, Sigma Aldrich, St. Louis, MO, USA), lauryl sulfate (L22010, Research Products International, Mt. Prospect, IL, USA), sodium chloride (S23020-1000.0, Research Products International, Mt. Prospect, IL, USA), TRIS base (T600400-1000.0, Research Products International, Mt. Prospect, IL, USA), glycine (G36050-1000.0, Research Products International, Mt. Prospect, IL, USA), methanol (A465-4, Fischer Chemical, Geel, Belgium), 30% acrylamide/bis solution 37.5:1 with 2.6% crosslinker (1610158, BIO RAD, Hercules, CA, USA), 10x Tris/Glycine/SDS running buffer (1610732, BIO RAD, Hercules, CA, USA), and blot paper (1703967, BIO RAD, Hercules, CA, USA).

After transfer, PVDF membranes were blocked in Intercept blocking buffer TBS (927-60001, LI-COR, Lincoln, NE, USA). Staining was done overnight at 4°C on a rocker with mouse anti-human vimentin monoclonal antibody (14-9897-82, Thermo Fischer Scientific, Milton Park, UK) diluted at a 1:500 ratio in the blocking buffer. GAPDH antibody (MAB374, EMD Millipore, Burlington, MA, USA) was used as a loading control diluted in blocking buffer at a ratio of 1:2000. The secondary antibodies used were IRDye 800CW goat anti-rabbit secondary antibody (926-32211, LICOR, Lincoln, Nebraska, USA) and

IRDye 800CW goat anti-mouse secondary antibody (926-32210, LICOR, Lincoln, Nebraska, USA) at a dilution of 2:15,000. Membranes were imaged with a LICOR Odyssey Fc (LICOR Biosciences, Lincoln, Nebraska, USA) and quantified with Image Studio software (LICOR Biosciences, Lincoln, Nebraska, USA) following the LICOR housekeeping protein normalization protocol. Values for the treatment groups were then normalized to the relative expression in the untreated cells grown on the 5kPa gels. Data analysis was performed on GraphPad Prism using an unpaired, parametric t-test where $p < 0.05$ was considered statistically significant. All values are presented as mean \pm SD.

Chapter 3: Results

3.1 Stiffer Substrates Lead to Increased Calcium Flux and Vimentin Expression

To address previous observations in the literature that increasing stiffness plays a role in intracellular free calcium modulation and is implicated in the progression of the EMT cell phenotype, the prostate cancer cell lines PC3 and DU145 were plated onto substrates of three different stiffnesses. The softest substrate was a PA gel with an elastic modulus of 5kPa, recapitulating the stiffness cells experience in healthy prostatic tissue (Correas et al., 2015). The second PA gel modeled the stiffness in an advanced stage prostate tumor which typically has a measured mean stiffness of 60kPa (Barr et al., 2012). Glass coverslips were used as a positive control for stiffness since it is effectively an infinitely stiff environment for the cells, as glass fibers exhibit a Young's modulus of about 72GPa.

Calcium flux in PC3 cells is heavily influenced by the stiffness of the substrate the cells are grown on, as seen in the micrographs in **Fig. 2B**. Cells grown on the soft PA gels showed a measured mean $\Delta F/F_0$ of 1.27 ± 0.09 (**Fig. 2C**). Comparatively, cells which were grown on the stiffer 60kPa gels and the glass control coverslips showed significantly increased mean intracellular $\Delta F/F_0$ of 1.86 ± 0.33 and 2.04 ± 0.24 , respectively. The $\Delta F/F_0$ of the cells on the two stiffer substrates were not statistically different from each other, suggesting that there is an upper limit to the mechanosensitivity of PC3 cells and subsequently a maximum threshold for calcium flux into the cells due to changing stiffness.

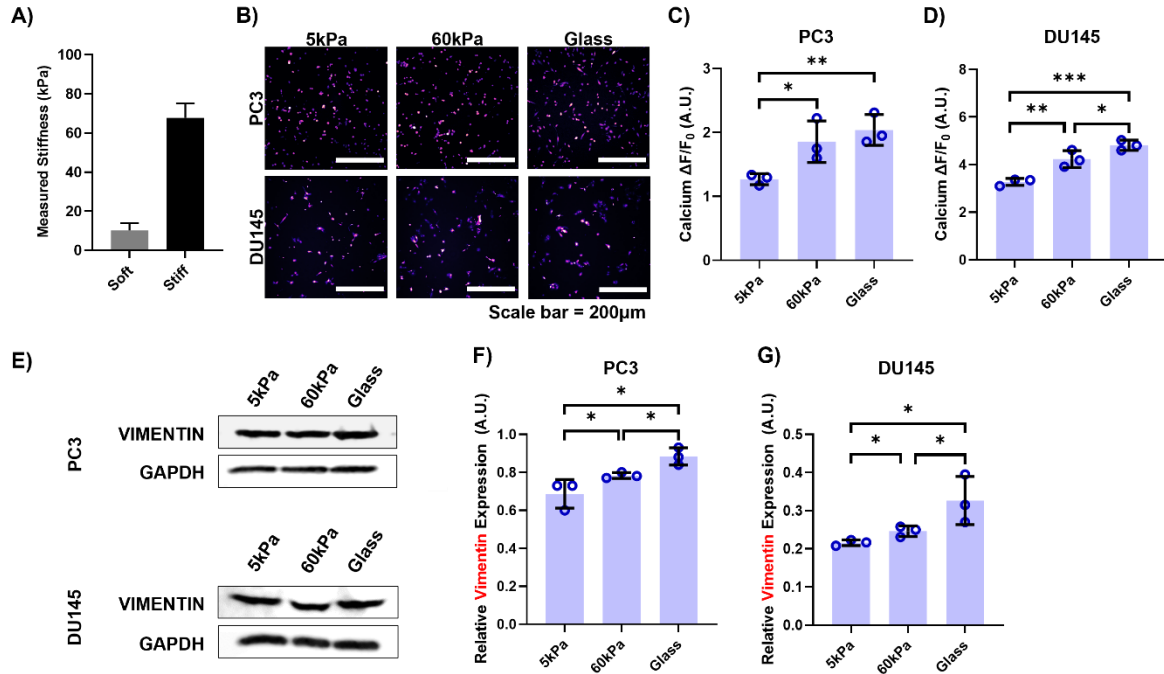


Figure 2. Effect of stiffness on intracellular calcium concentration and vimentin expression. **A)** Confirmation of PA gel stiffness via contact mode AFM, where each experiment consisted of 16 indentations to measure stiffness in a 120x120µm grid on each substrate (the figure shows the mean \pm SD for n=3 experiments). **B)** Micrographs displaying the increase of Fluo-4 mean fluorescence with stiffness. Quantification of the changes in intracellular calcium concentration in cells grown on 5kPa PA gels, 60kPa PA gels, and the glass control in **C)** PC3 cells and **D)** DU145 cells. **E)** Qualitative images of western blots showing increasing vimentin expression with matrix stiffness. Quantification of the changes in vimentin expression in the prostate cancer cell lines **F)** PC3 and **G)** DU145. Graphs display the mean \pm SD for n = 3 sample size. Statistical significance is shown as * for p<0.05, ** for p<0.01, *** for p<0.001, and **** for p<0.0001, as evaluated by unpaired, parametric t-tests.

Calcium flux into the DU145 cells showed similar sensitivity to substrate stiffness as the PC3 cells (**Fig. 2B & 2D**). Cells on the 60kPa gels and the glass control showed a 29.5% and 46.8% increase in calcium concentration, respectively, compared to cells grown on the softest PA gels. Notably, there was a significant difference in the measured $\Delta F/F_0$ between DU145 cells grown on the 60kPa gels and those on the glass coverslips. Matrix stiffness had a prominent effect on vimentin expression (**Fig. 2E**). In both cell lines, an increase in stiffness lead to higher vimentin expression, where each group was significantly different from each other (**Fig. 2F & 2G**). The PC3 cells showed a small but significant increase from the softer to the stiffer PA gels. A greater effect was seen when the cells were plated on the glass coverslip, where there was a 29% increase in vimentin expression compared to the 5kPa group. Consistently, the DU145 cells plated on the glass coverslips showed a 1.5-fold increase in vimentin expression compared to the cells grown on the softer PA gels. This is supported by other findings in the literature showing vimentin expression is known to increase dramatically with stiffness (Rice et al., 2017).

3.2 EMT Associated Characteristics Change with Stiffness

Results for the effect of matrix stiffness on cell shape and actin polymerization are shown in the micrographs in **Fig. 3A & 3B**, respectively. Cell aspect ratio is a common metric for assessing changes in cell morphology: an increasing aspect ratio is associated with cells losing their apico-basal polarity and elongating to take on a more mesenchymal-like phenotype (Leggett et al., 2016; Ondeck et al., 2019). Manual contours of cells were measured for their aspect ratio and cross-sectional area.

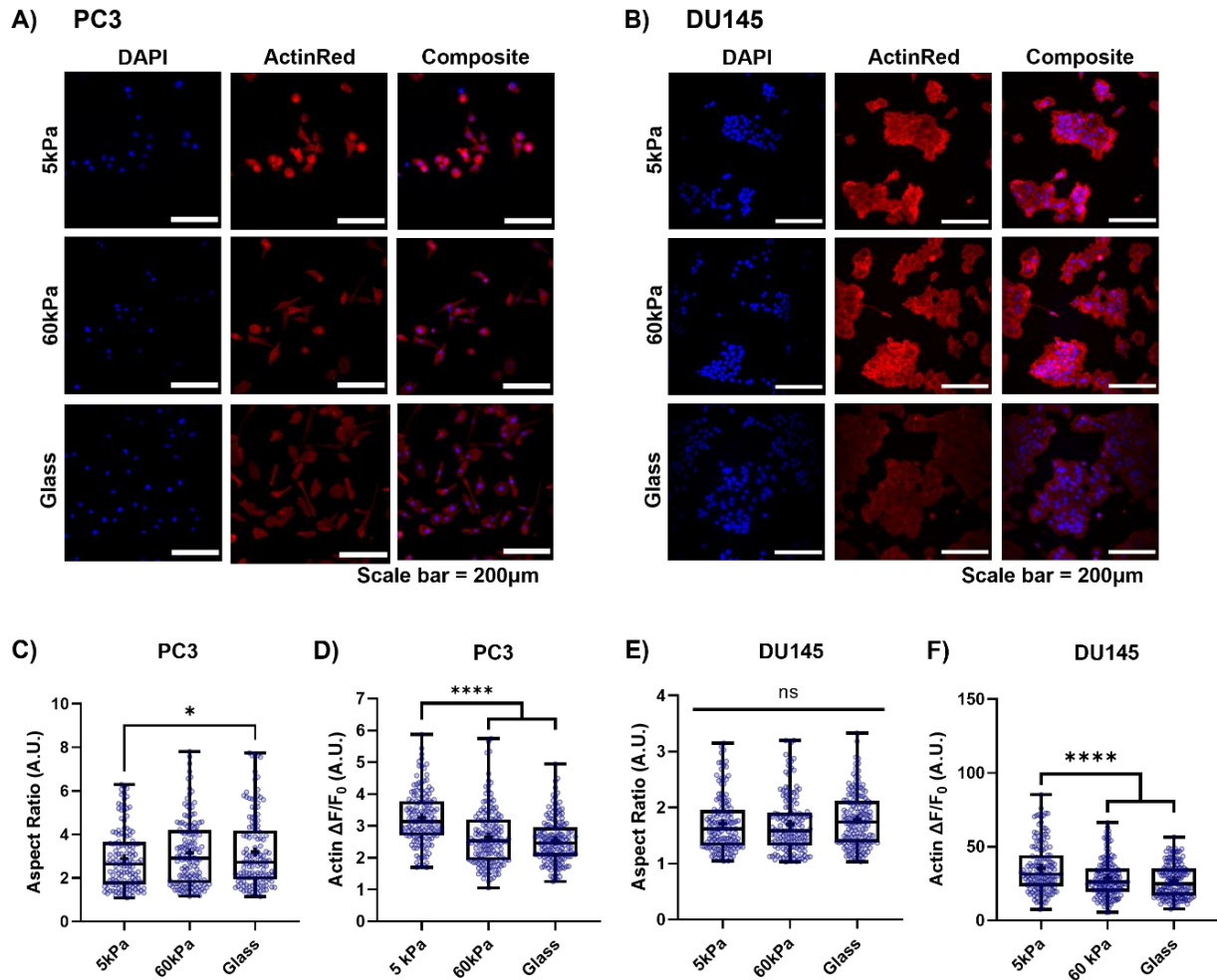


Figure 3. Effect of stiffness on EMT morphology in both PC3 and DU145 prostate cancer cells. Micrographs of **A) PC3** cells and **B) DU145** cells grown on the 3 different substrates and stained with ActinRed555 and DAPI. Measurements taken from the PC3 cell images of **C)** increases in aspect ratio and **D)** decreasing F-actin fluorescence with stiffness. Quantification of **E)** aspect ratio and **F)** F-actin fluorescence in the DU145 cell images. Graphs display the box plot from min to max of $n = 50$ sample size for each of the 3 biological replicates. Statistical significance is shown as * for $p < 0.05$, ** for $p < 0.01$, *** for $p < 0.001$, and **** for $p < 0.0001$, as evaluated by unpaired, parametric t-tests.

The mean aspect ratio of the PC3 cells increased with stiffness (**Fig. 3C**). With respect to aspect ratio, the difference was significant between the cells grown on the 5kPa gels and the glass control, and showed that, like the calcium flux, it begins to plateau at higher stiffnesses. A decreasing trend in F-actin fluorescence was observed with increasing stiffness, where cells grown on the softer gels showed significantly higher mean fluorescence than those grown on the stiffer gels (**Fig. 2D**). In contrast, the increases in matrix stiffness alone did not influence the aspect ratio of the DU145 cells (**Fig. 3E**). Interestingly, F-actin fluorescence in the DU145 cells decreased by 33% from the cells grown on the 5kPa PA gels to cells grown on both of the stiffer substrates (**Fig. 3F**).

3.3 Calcium Flux Depends on Treatment and Stiffness

To investigate how changes in calcium influx due to Piezo1 activation and inhibition affect important aspects of EMT, cells were treated with either Yoda1 or GsMTx-4 on each of the three substrates. Yoda1 is a specific pharmacological activator of Piezo1 (Botello-Smith et al., 2019). It decreases the mechanical threshold of activation of the channel by acting as a molecular wedge that allows for easier conformational changes due to deformation in the lipid bilayer. In contrast, GsMTx-4 can block Piezo1 and decrease calcium flux into the cell by stabilizing its closed state and therefore raising the energy barrier required to open the pore (Bae et al., 2011).

Changes in calcium flux due to treatments and matrix stiffness were confirmed by measurements of Fluo-4 fluorescence intensity via immunofluorescence microscopy.

Micrographs of the PC3 cells can be observed in **Fig. 4A**. The PC3 cells grown on the 5kPa (**Fig. 4B**) and 60kPa (**Fig. 4C**) PA gels showed significantly increased intracellular calcium concentration when treated with Yoda1 compared to the DMSO vehicle control. Specifically, Yoda1 increased the calcium flux by 35% in the cells grown on both the 5kPa and 60kPa gels. No difference was observed between the DMSO vehicle control and the Yoda1-treated cells on the glass control substrate (**Fig. 4D**).

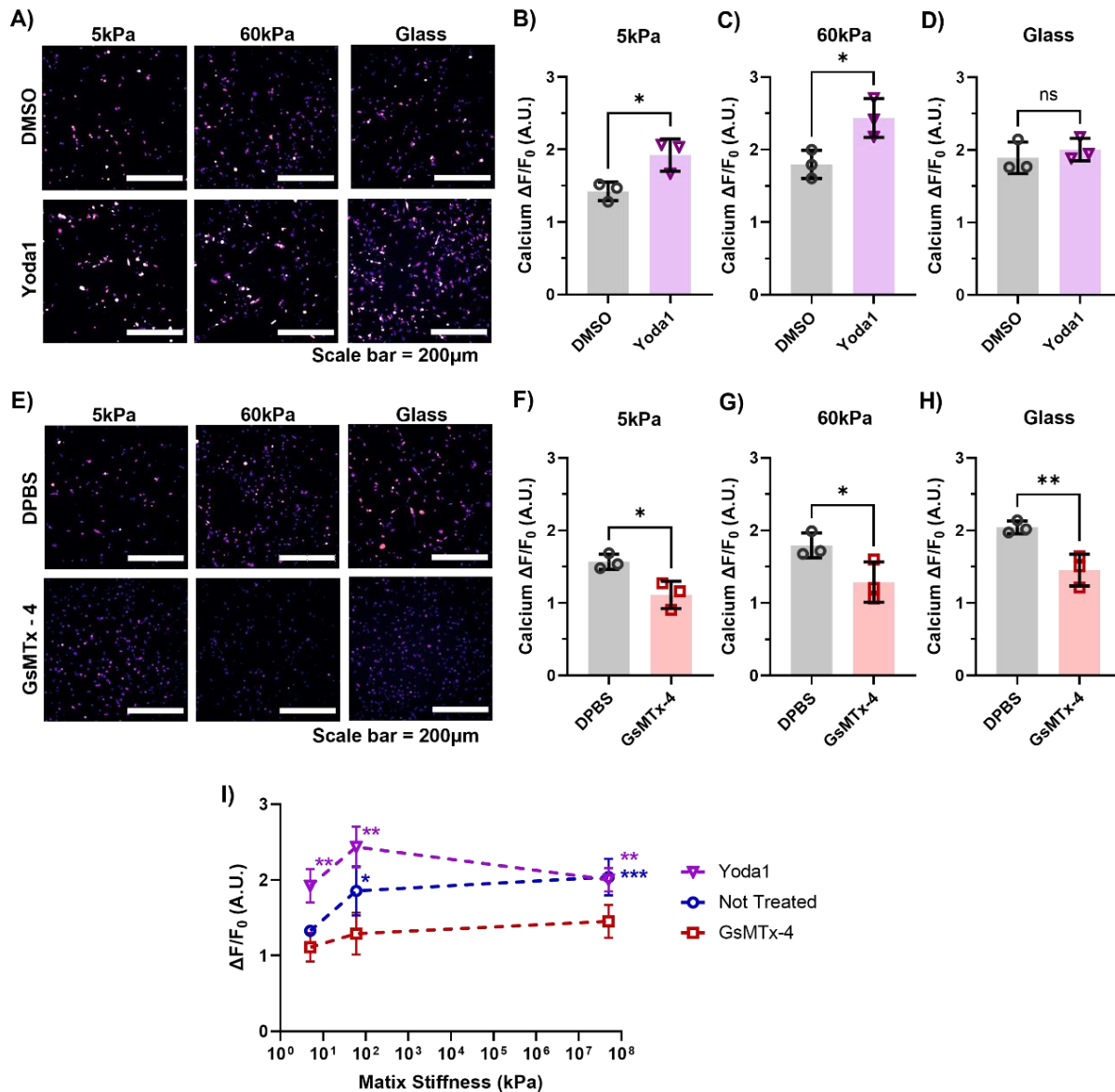


Figure 4. Effects of pharmacological activation and inhibition on intracellular calcium concentration in PC3 cells at different stiffnesses. A) Micrographs displaying Fluo-4 fluorescence of PC3 cells grown on 5kPa, 60kPa, and glass substrates and treated with Yoda1 or the DMSO vehicle control. Difference in intracellular calcium concentration between DMSO- and Yoda1- treated cells on **B)** 5kPa substrates, **C)** 60kPa substrates, and **D)** glass control. **E)** Micrographs of GsMTx-4 treated cells compared to the DPBS vehicle control on each of the 3 different matrices. Changes in $\Delta F/F_0$ with DPBS or GsMTx-4 treatment of cells on **F)** 5kPa substrates, **G)** 60kPa substrates, and **H)** glass control. **I)** Summary of pharmacological activation and inhibition of Piezo1 in soft and stiff gels, and the glass control compared to cells that did not receive any treatment. Graphs display the mean \pm SD for $n = 3$ sample size. Statistical significance is shown as * for $p < 0.05$, ** for $p < 0.01$, *** for $p < 0.001$, and **** for $p < 0.0001$, as evaluated by unpaired, parametric t-tests.

GsMTx-4 decreased the calcium flux in all three substrates, as shown in the micrographs in **Fig. 4E**. The cells that were grown on the 5kPa (**Fig. 4F**) and 60kPa (**Fig. 4G**) gels had significantly decreased intracellular calcium concentration when treated with GsMTx-4 compared to those treated with DPBS. The greatest difference was found in the cells incubated on the glass slides, where there was a 29% decrease in calcium flux between the DPBS vehicle control and the GsMTx-4 treatment (**Fig. 4H**).

The results are summarized in **Fig. 4I**, comparing the changes in cellular calcium flux between stiffnesses and treatment conditions. All the cells treated with Yoda1, on all substrate stiffness tested, had significantly increased intracellular calcium concentrations compared to the cells grown on the 5kPa gels without treatment. In comparison,

increasing matrix stiffness had no effect on calcium flux when the cells were treated with GsMTx-4. These all showed a comparable magnitude of $\Delta F/F_0$ as untreated cells grown on the 5kPa gels. The intracellular calcium concentration did plateau around $\Delta F/F_0 \approx 2.4$ and exhibited a lower bound at around $\Delta F/F_0 \approx 1.1$.

Piezo1 activation via the agonist Yoda1 had significant effects on DU145 cells grown on each of the three substrates in comparison to the DMSO vehicle control (**Fig. 5A**). On the 5kPa and 60kPa gels, the cells showed a 42% and 41% increase, respectively, in $\Delta F/F_0$ with Yoda1 treatment compared to the DMSO control (**Fig. 5B & 5C**). In the glass control group, the intracellular calcium concentration also changed significantly after Piezo1 activation (**Fig. 5D**), differing from the results observed for the PC3 cells. When the DU145 cells were treated with GsMTx-4, the changes in calcium concentration were comparable to those in the PC3 cells, especially on the stiffer substrates (**Fig. 5E**). Pharmacological inactivation of Piezo1 did not have a significant effect on $\Delta F/F_0$ in the cells grown on the softest substrate (**Fig. 5F**). When the cells were grown on both of the stiffer substrates however, there was a significant decrease in the intracellular calcium concentration in comparison to the DPBS vehicle control at the corresponding substrate stiffness (**Fig. 5G & 5H**).

Comparisons between the $\Delta F/F_0$ on different stiffnesses and treatments for the DU145 cells can be observed in **Fig. 5I**. In these cells, the effect of increasing stiffness on intracellular calcium concentration was less than in the PC3 cell line. Most noticeably, none of the untreated DU145 cells reached the intracellular calcium concentration as those cells treated with Yoda1, a phenomenon which was seen in the PC3 cells at the higher stiffnesses. Additionally, when the cells were treated with Yoda1 on the 5kPa gels,

they nearly reached the same magnitude of $\Delta F/F_0$ as those treated with Yoda1 on the stiffer substrates. Similarly to the PC3 cells, the DU145 cells treated with GsMTx-4 on both of the stiffer substrates did not have significantly different intracellular calcium concentrations to the untreated cells grown on the 5kPa PA gels. This finding suggests that they also had a lower bound for Piezo1 inactivation.

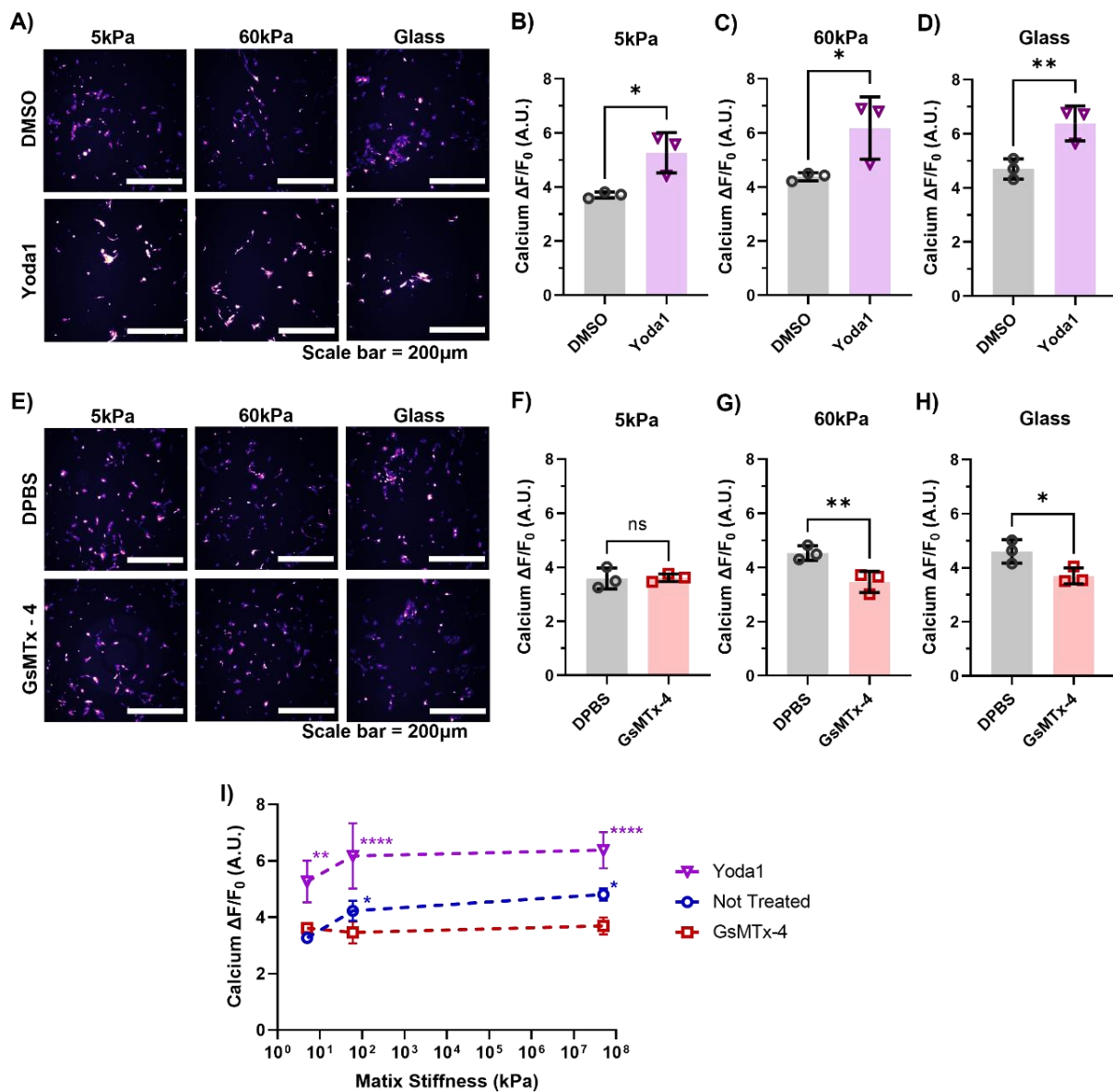
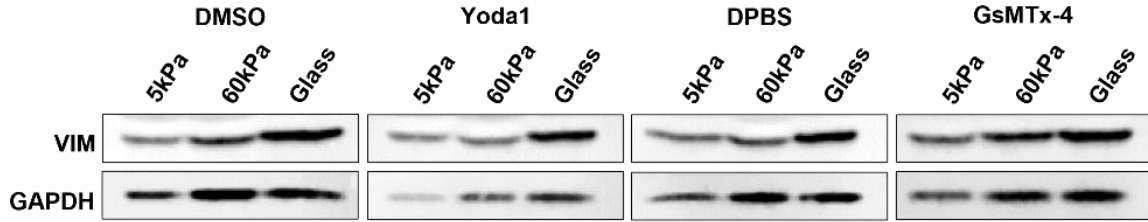


Figure 5. Effects of pharmacological activation and inhibition on intracellular calcium concentration at different stiffnesses in DU145 cells. **A)** Micrographs displaying Fluo-4 fluorescence of DU145 cells grown on 5kPa, 60kPa, and glass substrates and treated with Yoda1 or the DMSO vehicle control. Difference in intracellular calcium concentration between DMSO- and Yoda1- treated cells on **B)** 5kPa substrates, **C)** 60kPa substrates, and **D)** glass control. **E)** Micrographs of GsMTx-4 treated cells compared to the DPBS vehicle control on each of the 3 different matrices. Changes in $\Delta F/F_0$ with DPBS or GsMTx-4 treatment of cells on **F)** 5kPa substrates, **G)** 60kPa substrates, and **H)** glass control. **I)** Summary of pharmacological activation and inhibition of Piezo1 in soft and stiff gels, and the glass control compared to the cells that did not receive any treatment. Graphs display the mean \pm SD for $n = 3$ sample size. Statistical significance is shown as * for $p < 0.05$, ** for $p < 0.01$, *** for $p < 0.001$, and **** for $p < 0.0001$, as evaluated by unpaired, parametric t-tests.

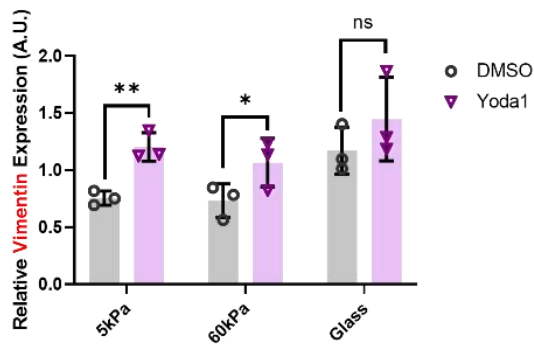
3.4 Effect of Yoda1 and GsMTx-4 on Vimentin Expression

Western blotting was performed after the cells were treated with either Yoda1 or GsMTx-4 to determine how the changes in Piezo1 activation would affect total vimentin expression. Qualitative western blot images of the effects of Piezo1 inhibition and activation on the prostate cancer cell line PC3 are shown in **Fig. 6A**. Following the trends in calcium concentration, cells grown in 5kPa gels and 60kPa gels had significant increases in vimentin expression when treated with Yoda1 compared to the DMSO vehicle control (**Fig. 6B**).

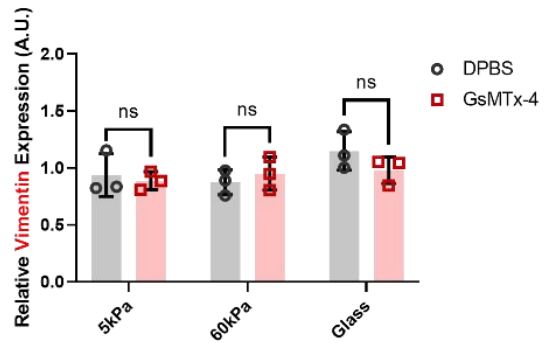
A) PC3



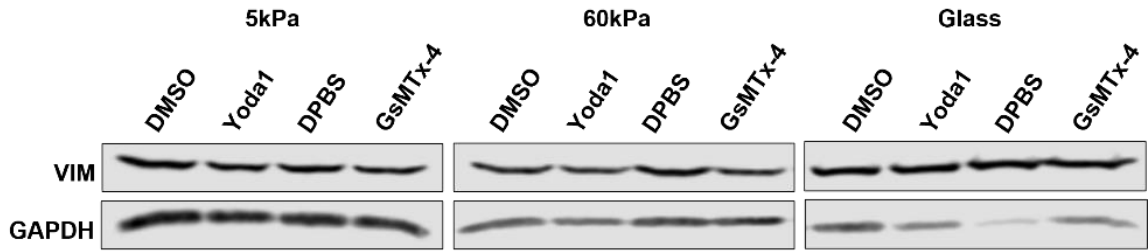
B)



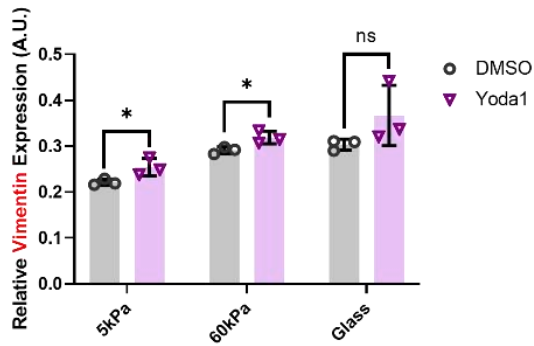
C)



D) DU145



E)



F)

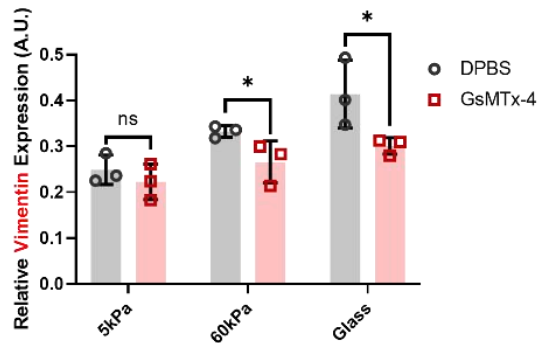


Figure 6. Western blots showing the effects of pharmacological activation and inhibition of Piezo1 on substrates of increasing stiffness on total vimentin expression in PC3 and DU145 cells. A) Qualitative images of the western blot results showing increasing vimentin expression in PC3 cells with matrix stiffness and Yoda1 treatments compared to the housekeeping protein GAPDH. **B)** Quantification of the western blot bands showing increasing vimentin expression in PC3 cells treated with the DMSO vehicle control and Yoda1 treatment. **C)** Effects of GsMTx-4 treatment on PC3 cells. **D)** Western blots showing the effects of pharmacological activation and inhibition of Piezo1 in DU145 cells grown on substrates of increasing stiffness on total vimentin expression. Quantification of the western blot bands showing vimentin expression in DU145 cells incubated on 5kPa PA gels, 60kPa PA gels after Piezo1 **E)** activation and **F)** inhibition. Graphs display the mean \pm SD for $n = 3$ sample size normalized to the not treated, 5kPa group. Statistical significance is shown as * for $p < 0.05$, ** for $p < 0.01$, *** for $p < 0.001$, and **** for $p < 0.0001$, as evaluated by unpaired, parametric *t*-tests.

Specifically, vimentin expression increased by 60% with Yoda1 treatment on the 5kPa gels. On the 60kPa gels, an increase of 45% in total vimentin expression was observed with Piezo1 activation. There was no difference in vimentin expression between the vehicle control and the Yoda1-treated cells on the glass control substrates. GsMTx-4 treatment did not have any effect on vimentin expression in the cells cultured on either the 5kPa gels or the 60kPa gels (**Fig. 6C**). On the glass substrates, a small decreasing trend was seen with GsMTx-4 treatment compared to the DPBS vehicle control group, but this change was not statistically significant.

Results from the western blots of DU145 cells grown on the three substrates and treated with either Yoda1 or GsMTx-4 can be seen in **Fig. 6D**. These cells reacted similarly to the PC3 cells to the Yoda1 activation at all three stiffness conditions (**Fig. 6E**). There was a small but significant increase in total vimentin expression between the Yoda1-treated cells and the DMSO control on both the 5kPa and 60kPa gels. Consistent with the PC3 results, there was no change in vimentin expression with Piezo1 activation in the glass control group. The DU145 cells were found to be more sensitive to the GsMTx-4 treatments than the PC3 cells, especially at the stiffer conditions (**Fig. 6F**). There was no significant change in vimentin expression between the vehicle control and treatment groups in the cells grown on the 5kPa gels. Interestingly, the cells on the 60kPa gel had a 25% decrease in vimentin expression after GsMTx-4 treatment compared to the DPBS control. This was also observed in the glass condition where there was 38% decrease between the GsMTx-4 treatment and the DPBS control.

3.5 Effect of Yoda1 and GsMTx-4 on EMT Morphology

Cells were stained with ActinRed555 to measure the changes in cell aspect ratio and filamentous actin (F-actin) fluorescence in response to the pharmacological activation of Piezo1 with Yoda1 at each of the different stiffnesses. Micrographs of the PC3 cells are shown in **Fig. 7A**. With respect to aspect ratio, Yoda1 had the greatest effect on the cells grown on the 5kPa gels (**Fig. 7B**). At this stiffness condition, cells were treated with the Piezo1 agonist were significantly more spindle-like and elongated than those in the vehicle control group. In comparison, the cells grown on the 60kPa gels and the glass

control showed no significant changes in aspect ratio compared to the control. A decrease in F-actin fluorescence was observed at all stiffnesses when the cells were treated with Yoda1 (**Fig. 7C**). This trend was particularly defined at the 5kPa condition, where the F-actin fluorescence decreased by 20% when the cells were treated with Yoda1. Compared to the DMSO control, cells on the 60kPa gels and the glass control decreased by 13% and 18% in mean F-actin fluorescence, respectively.

GsMTx-4 treatment had a less pronounced effect on cell aspect ratio and F-actin fluorescence, as exhibited by the micrographs in **Fig. 7D**. No difference in aspect ratio was observed in the cells grown on 5kPa gels between the control and GsMTx-4 treatment groups (**Fig. 7E**). Slight decreases were measured between the cells incubated on 60kPa gels and the glass controls, but this trend was not significant. In terms of the F-actin expression, the cells on the 5kPa gels treated with the vehicle control had no significant difference compared to those treated with GsMTx-4 (**Fig. 7F**). Interestingly, on the 60kPa gels, when PC3 cells were treated with GsMTx-4 there was a significant increase of about 12% in F-actin fluorescence compared to the DPBS vehicle control group. A similar trend was observed in the cells cultured on the glass coverslips, although this change was not statistically significant.

The effects of the pharmacological activation of Piezo1 and increasing substrate stiffness were prominent on DU145 cell morphology (**Fig. 8A**). Yoda1 treatment led to a more mesenchymal-like cell shape in the DU145 cell line compared to the DMSO vehicle control (**Fig. 8B**). A slight increase was observed in the aspect ratio of the cells grown on the 5kPa gels when treated with Yoda1 compared to the control, however this difference was not significant.

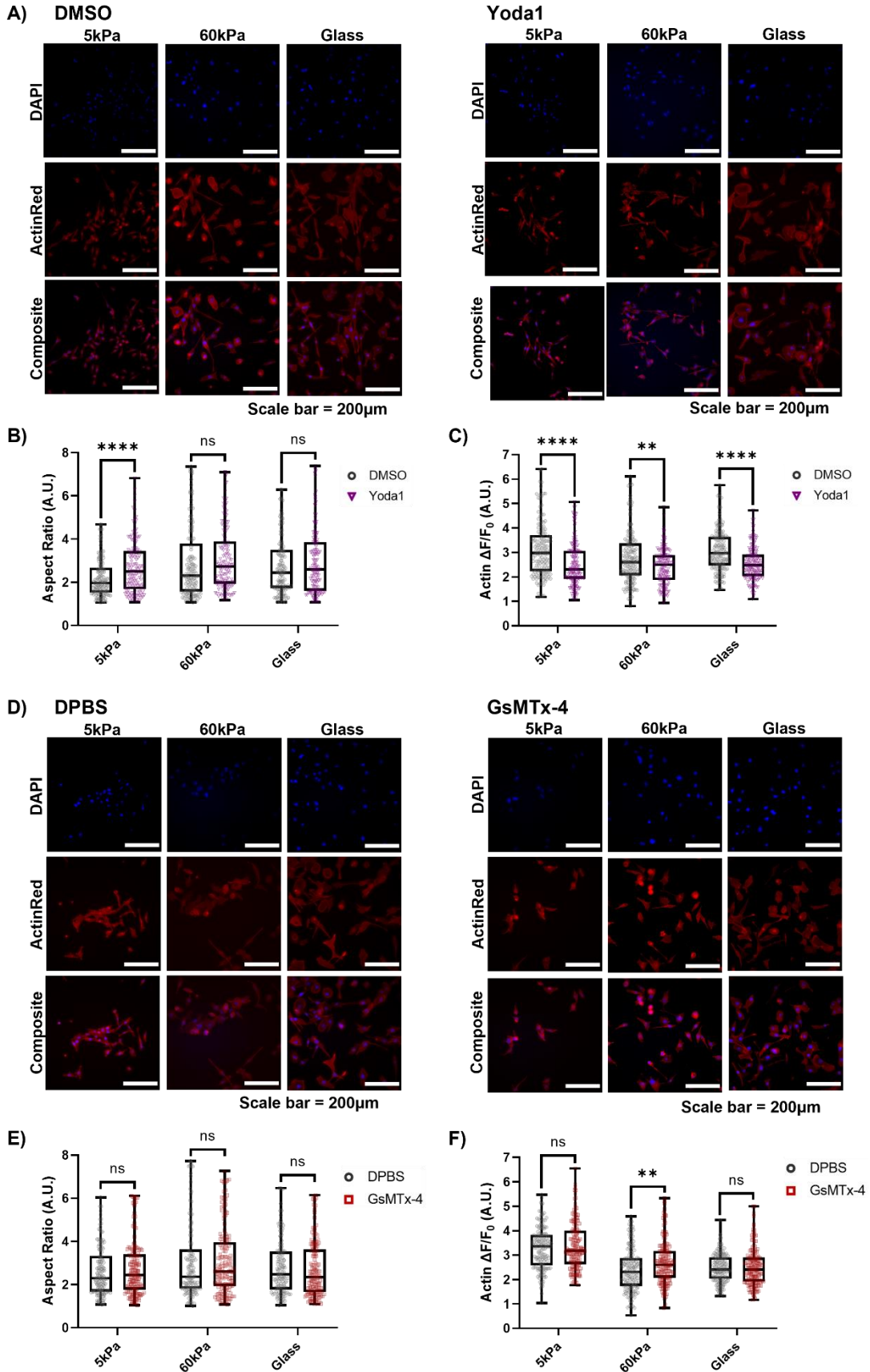


Figure 7. Changes in PC3 aspect ratio and F-actin fluorescence with stiffness and pharmacological activation and inhibition of Piezo1. **A)** Micrographs showing PC3 cells on soft and hard PA gels, as well as the glass control stained with ActinRed555 and DAPI after treatments with the DMSO vehicle control and Yoda1. **B)** Measurement of the aspect ratio of cells incubated on 5kPa PA gels, 60kPa PA gels, and the glass control comparing Yoda1 treatment to the vehicle control. **C)** Quantification of decreasing F-actin fluorescence with Yoda1 treatment compared to the DMSO vehicle control in the PC3 cells on each substrate. **D)** Micrographs showing PC3 cells after treatments with the DPBS vehicle control and GsMTx-4 grown on soft and hard PA gels, as well as the glass control, then stained with ActinRed555 and DAPI. **E)** Measurement of the aspect ratio of cells comparing GsMTx-4 treatment to the vehicle control at each stiffness. **F)** Quantification of decreasing F-actin fluorescence with GsMTx-4 treatment compared to the DPBS vehicle control in the PC3 cells. Graphs display the box plot from min to max of $n = 50$ sample size for each of the 3 biological replicates. Statistical significance is shown as * for $p < 0.05$, ** for $p < 0.01$, *** for $p < 0.001$, and **** for $p < 0.0001$, as evaluated by unpaired, parametric t-tests.

A significant increase in aspect ratio was seen in both groups of cells grown on the 60kPa gels and the glass controls with Yoda1 treatment. F-actin polymerization exhibited a more noticeable change with Yoda1 treatment (**Fig. 8C**). In the DU145 cells grown on the 5kPa gels, the F-actin $\Delta F/F_0$ was 46% lower in the treatment group compared to the vehicle control. Cells grown on both of the stiffer substrates also displayed significant decreases in F-actin with Yoda1 treatment, although these were not as pronounced as in the softer gels.

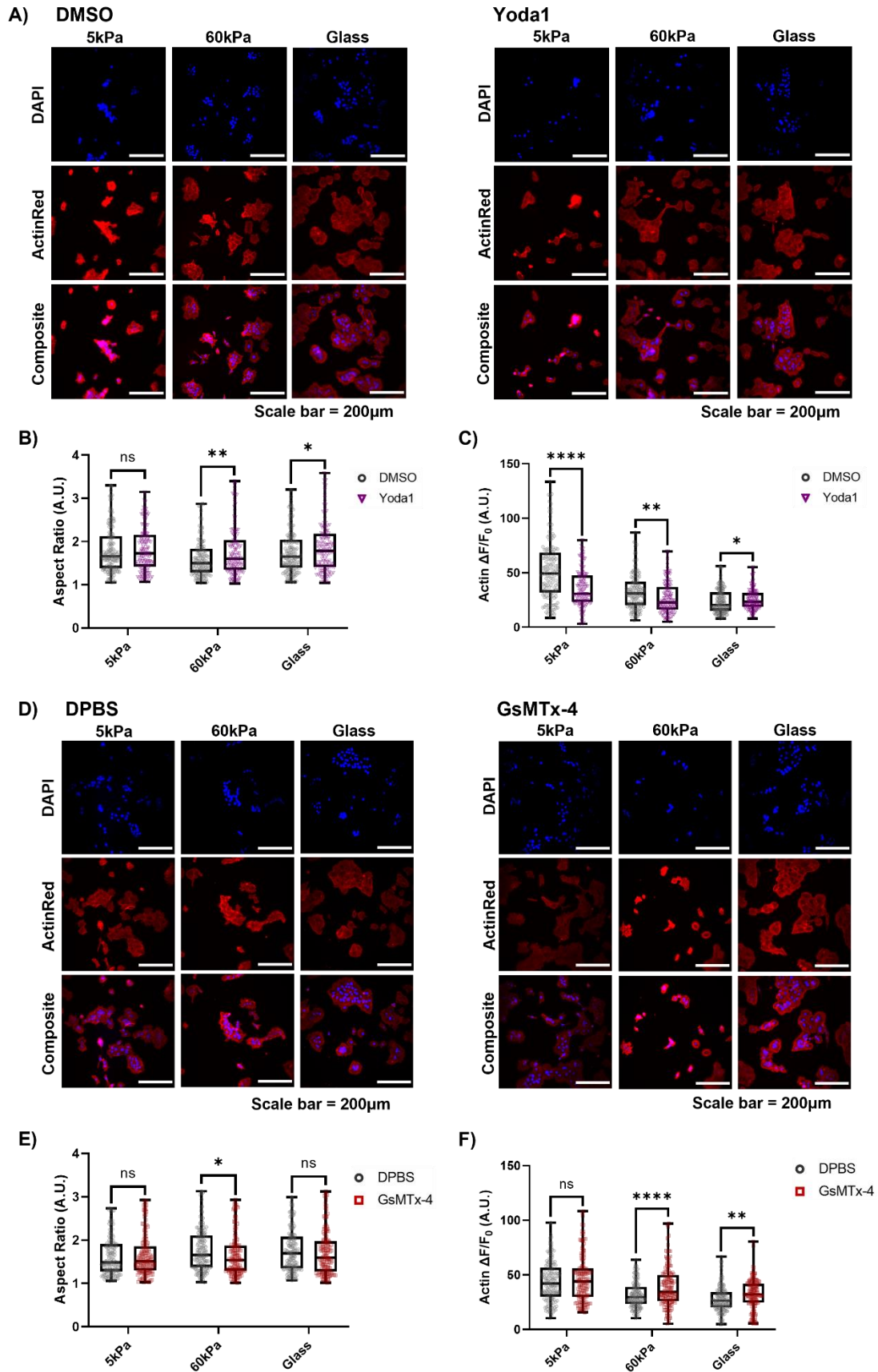


Figure 8. Effects of Yoda 1 and GsMTx-4 treatment on the aspect ratio and F-actin fluorescence of DU145 cells incubated on substrates of increasing stiffness. A) Micrographs showing DU145 cells on soft and hard PA gels, as well as the glass control stained with ActinRed555 and DAPI after treatments with the DMSO vehicle control and Yoda1. **B)** Measurement of the aspect ratio of cells incubated on 5kPa PA gels, 60kPa PA gels, and the glass control comparing Yoda1 treatment to the vehicle control. **C)** Quantification of decreasing F-actin fluorescence with Yoda1 treatment compared to the DMSO vehicle control in the DU145 cells on each substrate. **D)** Micrographs showing DU145 cells after treatments with the DPBS vehicle control and GsMTx-4 grown on soft and hard PA gels, as well as the glass control, then stained with ActinRed555 and DAPI. **E)** Measurement of the aspect ratio of cells comparing GsMTx-4 treatment to the vehicle control at each stiffness. **F)** Quantification of decreasing F-actin fluorescence with GsMTx-4 treatment compared to the DPBS vehicle control in the DU145 cells. Graphs display the box plot from min to max of $n = 50$ sample size for each of the 3 biological replicates. Statistical significance is shown as * for $p < 0.05$, ** for $p < 0.01$, *** for $p < 0.001$, and **** for $p < 0.0001$, as evaluated by unpaired, parametric *t*-tests.

Consistent with the western blot results, the DU145 cells were found to be more sensitive to the GsMTx-4 treatment than the PC3 cells (**Fig. 8D**) with respect to aspect ratio and F-actin polymerization. On the 5kPa substrates, there were no changes in the cell aspect ratio between the treatment and control group (**Fig. 8E**). As the stiffness increased to 60kPa, the aspect ratio showed a significant decrease with Piezo1 inhibition

compared to the DPBS control. This trend was also observed in the glass control surface, although this was not a significant difference. F-actin fluorescence trended in a similar manner. $\Delta F/F_0$ increased significantly under both the 60kPa and glass control conditions when the cells were treated with GsMTx-4 compared to the vehicle control (**Fig. 8F**). As reported above, the cells F-actin polymerization in the DU145 cells did not change with treatment in the 5kPa gels.

Chapter 4: Discussion

Changes in intracellular calcium concentrations are known to govern several important processes in cancer cells linked to disease progression, including increased proliferation, migration, invasion, resistance to apoptosis, and angiogenesis (Holt et al., 2020; Kaur and Sanyal, 2011; Pla et al., 2010, 2012; Stewart et al., 2015; Zhu et al., 2014). Cells have the ability to modulate calcium flux into the intracellular space via mechanosensitive ion channels in the membrane, such as Piezo1 (Coste et al., 2010). Piezo1 is opened by tension in the cell membrane as the matrix resists deformation when a cell pulls on it to migrate (Janmey et al., 2019). The present study connects how the increases in calcium concentration via Piezo1 activation due to increased matrix stiffness can lead to increased EMT in the prostate cancer cell lines PC3 and DU145 (**Fig. 1**). This environment was modeled by polymerizing PA gels of 5kPa and 60kPa which recapitulated the stiffnesses of healthy prostatic tissue and prostate cancer tumor, respectively (**Fig. 2A**).

Most cells in the human body are acutely sensitive to changes in intracellular calcium concentrations, as this governs most aspects of cellular life (Clapham, 2007). Cells utilize calcium pumps as one of the main signaling mechanisms to sense changes in the extracellular space and convert these to reactions in the intracellular domain (Hope et al., 2018). Once inside the cell, calcium regulates several signaling networks. It is heavily involved in mitochondrial health and function, innate immunity, and cellular apoptosis pathways, which are sensitive to nano- to micro-molar scale changes in intracellular calcium concentration. As a result, the observed changes in calcium fluorescence in the

PC3 and DU145 cell lines due to changing stiffness are notable, even if they were only elevated 50 to 60% over the cells grown on the soft substrate to those on the stiffer substrates (**Fig. 2B, 2C, & 2D**). Notably, the DU145 cells were not found to be as sensitive to changes in matrix stiffness alone as the PC3 cells. This could be due to the fact that DU145 cells have been seen to have a higher stiffness themselves than the PC3 cells, therefore possibly having the ability to resist deformation to a greater extent (Hope et al., 2021).

In its resting state, Piezo1 takes on an inverted dome shape, storing potential energy in this way (Coste et al., 2012). As cells migrate, they will pull against the matrix, which resists deformation proportionally to its stiffness. This response creates lateral membrane tension leading to Piezo1 transitioning into its open state by flattening proportionally. When the PC3 cells were plated on the stiffer substrates, the measured calcium fluorescence plateaued, suggesting that the calcium channel had likely reached a maximum open state due to the resistance of substrates to deform (**Fig. 2C**). Yoda1 acts as a molecular wedge, decreasing the mechanical threshold for activation to increase the flow of calcium through the pore (Botello-Smith et al., 2019). Therefore, when cells were treated with Yoda1 on the soft substrates, the calcium fluorescence increased significantly compared to the vehicle control (**Fig. 4A, 4B, 4I, 5A, 5B, & 5I**). When the PC3 cells were incubated on the stiffer substrates, treatment with Yoda1 did not increase calcium influx since this had likely already reached a maximum open state (**Fig. 4C, & 4D**). In contrast, DU145 cells did not seem to reach a maximum open state in the glass coverslips since Yoda1 treatment saw a significant increase in calcium $\Delta F/F_0$ in this stiffness condition. Again, this supports the conclusion that the higher cell stiffness was

not able to fully activate Piezo1, therefore leaving room for further increasing calcium flux via the treatment (**Fig. 5C, 5D, & 5I**). Conversely, GsMTx-4 gates Piezo1 to stabilize its closed state, in this way raising the energy barrier required to open the pore and decrease calcium flux into the cell (Bae et al., 2011). Therefore, it was able to reduce the calcium flux into the cells on all three substrates stiffnesses, especially on the stiffer gels where Piezo1 showed more activity (**Fig. 5E-H, 5E-H**).

Vimentin expression and aspect ratio are two factors that have been heavily linked to EMT characterization in cancerous cells. In a study by *Leggett et al*, a modeling approach to EMT characterization based on vimentin expression and cytoplasm elongation was developed (Leggett et al., 2016). These morphological features were sufficient to accurately predict EMT phenotype in single cell analysis. By treating PC3 and DU145 cells with Yoda1, increases in both vimentin expression (**Fig. 6A, 6B, 6D, & 6E**) and aspect ratio (**Fig. 7A, 7B, 8A, & 8B**) were observed compared to cells incubated with DMSO when grown on the softer substrates. Similar results were observed in the groups that had no treatment and only stiffness increased (**Fig. 2E-G, 2A-C, & 3E**). Significant changes in vimentin expression and aspect ratio were not observed between the vehicle control and Yoda1 treatment on the glass control due to the already advanced stage of EMT that high stiffness environments can induce on their own.

Two of the main cellular cytoskeletal elements are the actin stress fibers and vimentin intermediate filaments. These govern motility and structural integrity while working in concert, and heavily influence each other (Jiu et al., 2017). The study by *Jiu et al* sheds light on how actin stress fiber assembly can be inhibited by vimentin filaments, and how knocking out vimentin via siRNAs will increase F-actin fluorescence. The results

showing the decreasing F-actin fluorescence with increasing stiffness can be seen in **Fig. 3D & 3F** in both cell lines. Additionally, the increases in vimentin expression with Yoda1 treatment compared to the vehicle control correlate with the decreases in F-actin fluorescence (**Fig. 7C & 8C**).

Pharmacologically inhibiting or knocking down the calcium channel TRPV4 are both known to both prevent EMT morphology in breast cancer even at higher matrix stiffnesses (Sharma et al., 2019). These effects were seen in DU145 cells when the vimentin expression (**Fig. 6F**), aspect ratio (**Fig. 8D & 8E**), and F-actin fluorescence (**Fig. 8F**) were quantified. Interestingly, these trends were not observed when the PC3 cells were treated with GsMTX-4 in the high stiffness substrates. In these groups, no significant changes on aspect ratio, F-actin fluorescence, or vimentin expression were observed (**Fig. 6C, 7D, 7E, & 7F**). This finding could be due to alternative integrin signaling pathways becoming activated with the high substrate stiffness and circumventing the pharmacological inhibition of Piezo1 (Levental et al., 2009). EMT and mechanotransduction are highly multidimensional and complex processes which rely on several different mechanisms to take place (Kalli and Stylianopoulos, 2018; Wullkopf et al., 2018). Piezo1 activation had profound effects in promoting EMT characteristics, yet its pharmacological inhibition did not have an effect. Therefore, it can be assumed that it is an important component in cell sensing of the matrix stiffness and the subsequent activation of EMT pathways but is not solely responsible for this sensing.

Interestingly, when cells are exposed to fluid stress in the circulation, the forces they experience lead to increases in intracellular calcium concentration in many different cell types, including cancer (Chow et al., 1992; Kamioka et al., 2006; Yamamoto et al.,

2000; Yankaskas et al., 2021). The study by *Choi et al* demonstrated that the high shear forces in the circulation were linked to increased EMT in circulating tumor cells isolated from breast cancer patients (Choi et al., 2019). Here, shear stress was found to be a critical factor in the EMT conversion, leading to increased mesenchymal markers and increased tumor growth in an orthotopic mouse model of breast cancer. A parallel can be drawn from that work to this study, as it supports the hypothesis that forces from the extracellular environment cause changes in calcium influx thus leading to EMT.

Conclusion

In this study, the biophysical environment of a prostate cancer tumor was modeled using PA gels which recapitulated the different stiffnesses observed during disease progression. The prostate cancer cell lines PC3 and DU145 were used to study the effects that the changes in stiffness had on EMT by Piezo1 modulation of calcium flux. It was seen in both cell lines that pharmacologically activating Piezo1 via Yoda1 treatment led to greater intracellular calcium concentrations, higher vimentin expression, increased aspect ratio, and lower F-actin fluorescence, especially in the softer PA gel condition. The opposite effect was seen in the stiffer substrates when cells were treated with the Piezo1 antagonist GsMTx-4. Overall, this study concludes that Piezo1 regulated calcium flux plays a role in cancer metastasis by sensing changes in ECM stiffness and modulating EMT markers.

References

Bae, C., Sachs, F., Gottlieb, P.A. (2011). The mechanosensitive ion channel Piezo1 is inhibited by the peptide GsMTx4. *Biochem.* **50**, 6295–6300.

Barr, R.G., Memo, R., Schaub, C.R. (2012). Shear wave ultrasound elastography of the prostate: initial results. *Ultrasound Q.* **28**, 13–20.

Bauer, J., Emon, M.A.B., Staudacher, J.J., Thomas, A.L., Zessner-Spitzenberg, J., Mancinelli, G., Krett, N., Saif, M.T., Jung, B. (2020). Increased stiffness of the tumor microenvironment in colon cancer stimulates cancer associated fibroblast-mediated prometastatic activin A signaling. *Sci Rep.* **10**, 50.

Botello-Smith, W.M., Jiang, W., Zhang, H., Ozkan, A.D., Lin, Y.-C., Pham, C.N., Lacroix, J.J., Luo, Y. (2019). A mechanism for the activation of the mechanosensitive Piezo1 channel by the small molecule Yoda1. *Nat Commun.* **10**, 4503.

Califano, J.P., Reinhart-King, C.A. (2008). A Balance of Substrate Mechanics and Matrix Chemistry Regulates Endothelial Cell Network Assembly. *Cel. Mol. Bioeng.* **1**, 122.

Chen, W., Park, S., Patel, C., Bai, Y., Henary, K., Raha, A., Mohammadi, S., You, L., Geng, F. (2021). The migration of metastatic breast cancer cells is regulated by matrix stiffness via YAP signaling. *Heliyon.* **7**, e06252.

Choi, H.Y., Yang, G.-M., Dayem, A.A., Saha, S.K., Kim, K., Yoo, Y., Hong, K., Kim, J.-H., Yee, C., Lee, K.-M., et al. (2019). Hydrodynamic shear stress promotes epithelial-mesenchymal transition by downregulating ERK and GSK3 β activities. *Breast Cancer Res.* **21**, 6.

Chow, T.W., Hellums, J.D., Moake, J.L., Kroll, M.H. (1992). Shear stress-induced von Willebrand factor binding to platelet glycoprotein Ib initiates calcium influx associated with aggregation. *Blood*. **80**, 113–120.

Clapham, D.E. (2007). Calcium Signaling. *Cell*. **131**, 1047–1058.

Correas, J.-M., Tissier, A.-M., Khairoune, A., Vassiliu, V., Méjean, A., Hélénon, O., Memo, R., Barr, R.G. (2015). Prostate Cancer: Diagnostic Performance of Real-time Shear-Wave Elastography. *Radiology*. **275**, 280–289.

Coste, B., Mathur, J., Schmidt, M., Earley, T.J., Ranade, S., Petrus, M.J., Dubin, A.E., Patapoutian, A. (2010). Piezo1 and Piezo2 are essential components of distinct mechanically-activated cation channels. *Science*. **330**, 55-60.

Coste, B., Xiao, B., Santos, J.S., Syeda, R., Grandl, J., Spencer, K.S., Kim, S.E., Schmidt, M., Mathur, J., Dubin, A.E., et al. (2012). Piezo proteins are pore-forming subunits of mechanically activated channels. *Nature*. **483**, 176–181.

Denisin, A.K., Pruitt, B.L. (2016). Tuning the Range of Polyacrylamide Gel Stiffness for Mechanobiology Applications. *ACS Appl. Mater. Interfaces*. **8**, 21893–21902.

Dombroski, J.A., Hope, J.M., Sarna, N.S., King, M.R. (2021). Channeling the Force: Piezo1 Mechanotransduction in Cancer Metastasis. *Cells*. **10**, 2815.

Emon, B., Bauer, J., Jain, Y., Jung, B., Saif, T. (2018). Biophysics of Tumor Microenvironment and Cancer Metastasis - A Mini Review. *Compt. Struct. Biotechnol. J.* **16**, 279–287.

Fang, X.Z., Zhou, T., Xu, J.Q., Wang, Y.X., Sun, M.M., He, Y.J., Pan, S.W., Xiong, W., Peng, Z.K., Gao, X.H., et al. (2021). Structure, kinetic properties and biological function of mechanosensitive Piezo channels. *Cell Biosci.* **11**, 13.

Gallagher, S.R. (2007). One-Dimensional SDS Gel Electrophoresis of Proteins. *Curr. Protoc. Mol. Bio.* **37**.

Han, Y., Liu, C., Zhang, D., Men, H., Huo, L., Geng, Q., Wang, S., Gao, Y., Zhang, W., Zhang, Y., et al. (2019). Mechanosensitive ion channel Piezo1 promotes prostate cancer development through the activation of the Akt/mTOR pathway and acceleration of cell cycle. *Int. J. Oncol.* **55**.

Heerboth, S., Housman, G., Leary, M., Longacre, M., Byler, S., Lapinska, K., Willbanks, A., Sarkar, S. (2015). EMT and tumor metastasis. *Clin. Transl. Med.* **4**, 6.

Holt, J.R., Zeng, W.-Z., Evans, E.L., Woo, S.-H., Ma, S., Abuwarda, H., Loud, M., Patapoutian, A., Pathak, M.M. (2021). Spatiotemporal dynamics of PIEZO1 localization controls keratinocyte migration during wound healing. *eLife.* **10**, e65415.

Hope, J., Greenlee, J., King, M.R. (2018). Mechanosensitive Ion Channels: TRPV4 and P2X7 in Disseminating Cancer Cells. *Cancer J.* **24**, 84–92.

Hope, J.M., Bersi, M.R., Dombroski, J.A., Clinch, A.B., Pereles, R.S., Merryman, W.D., King, M.R. (2021). Circulating prostate cancer cells have differential resistance to fluid shear stress-induced cell death. *J. Cell Sci.* **134**.

Hope, J.M., Lopez-Cavestany, M., Wang, W., Reinhart-King, C.A., King, M.R. (2019). Activation of Piezo1 sensitizes cells to TRAIL-mediated apoptosis through mitochondrial outer membrane permeability. *Cell Death & Disease.* **10**, 837.

- Janmey, P.A., Fletcher, D.A., Reinhart-King, C.A.** (2019). Stiffness Sensing by Cells. *Physiol. Rev.* **100**, 695–724.
- Ji, Y., Ruan, L., Ren, W., Dun, G., Liu, J., Zhang, Y., Wan, Q.** (2019). Stiffness of prostate gland measured by transrectal real-time shear wave elastography for detection of prostate cancer: a feasibility study. *BR. J. Radiol.* **92**, 20180970.
- Jiu, Y., Peränen, J., Schaible, N., Cheng, F., Eriksson, J.E., Krishnan, R., Lappalainen, P.** (2017). Vimentin intermediate filaments control actin stress fiber assembly through GEF-H1 and RhoA. *J. Cell Sci.* **130**, 892-902.
- Jolly, M.K., Ware, K.E., Gilja, S., Somarelli, J.A., Levine, H.** (2017). EMT and MET: necessary or permissive for metastasis? *Mol. Oncol.* **11**, 755–769.
- Kalli, M., Stylianopoulos, T.** (2018). Defining the Role of Solid Stress and Matrix Stiffness in Cancer Cell Proliferation and Metastasis. *Front. Oncol.* **8**, 55.
- Kalluri, R., Weinberg, R.A.** (2009). The basics of epithelial-mesenchymal transition. *J Clin. Invest.* **119**, 1420–1428.
- Kamioka, H., Sugawara, Y., Murshid, S.A., Ishihara, Y., Honjo, T., Takano-Yamamoto, T.** (2006). Fluid shear stress induces less calcium response in a single primary osteocyte than in a single osteoblast: implication of different focal adhesion formation. *J. Bone Miner. Res.* **21**, 1012–1021.
- Kaur, J., Sanyal, S.N.** (2011). Intracellular pH and calcium signaling as molecular targets of diclofenac-induced apoptosis against colon cancer. *Eur. J. Cancer Prev.* **20**, 263–276.

Leggett, S.E., Sim, J.Y., Rubins, J.E., Neronha, Z.J., Williams, E.K., Wong, I.Y. (2016). Morphological single cell profiling of the epithelial–mesenchymal transition. *Integr. Biol.* **8**, 1133–1144.

Levental, K.R., Yu, H., Kass, L., Lakins, J.N., Egeblad, M., Erler, J.T., Fong, S.F.T., Csiszar, K., Giaccia, A., Wenginger, W., et al. (2009). Matrix Crosslinking Forces Tumor Progression by Enhancing Integrin Signaling. *Cell.* **139**, 891–906.

Lin, Y.-C., Guo, Y.R., Miyagi, A., Levring, J., MacKinnon, R., Scheuring, S. (2019). Force-induced conformational changes in Piezo1. *Nature.* **573**, 230–234.

Ondeck, M.G., Kumar, A., Placone, J.K., Plunkett, C.M., Matte, B.F., Wong, K.C., Fattet, L., Yang, J., Engler, A.J. (2019). Dynamically stiffened matrix promotes malignant transformation of mammary epithelial cells via collective mechanical signaling. *Proc. Natl. Acad. Sci.* **116**, 3502–3507.

Pla, A.F., Genova, T., Pupo, E., Tomatis, C., Genazzani, A., Zaninetti, R., Munaron, L. (2010). Multiple Roles of Protein Kinase A in Arachidonic Acid–Mediated Ca²⁺ Entry and Tumor-Derived Human Endothelial Cell Migration. *Mol. Cancer Res.* **8**, 1466–1476.

Pla, F.A., Ong, H.L., Cheng, K.T., Brossa, A., Bussolati, B., Lockwich, T., Paria, B., Munaron, L., Ambudkar, I.S. (2012). TRPV4 mediates tumor-derived endothelial cell migration via arachidonic acid-activated actin remodeling. *Oncogene.* **31**, 200–212.

Rice, A.J., Cortes, E., Lachowski, D., Cheung, B.C.H., Karim, S.A., Morton, J.P., del Río Hernández, A. (2017). Matrix stiffness induces epithelial–mesenchymal transition and promotes chemoresistance in pancreatic cancer cells. *Oncogenesis.* **6**, e352–e352.

Roche, J. (2018). The Epithelial-to-Mesenchymal Transition in Cancer. *Cancers.* **10**, 52.

Rouvière, O., Melodelima, C., Hoang Dinh, A., Bratan, F., Pagnoux, G., Sanzalone, T., Crouzet, S., Colombel, M., Mège-Lechevallier, F., Souchon, R. (2017). Stiffness of benign and malignant prostate tissue measured by shear-wave elastography: a preliminary study. *Eur Radiol.* **27**, 1858–1866.

Schrader, J., Gordon-Walker, T.T., Aucott, R.L., Deemter, M. van, Quaas, A., Walsh, S., Benten, D., Forbes, S.J., Wells, R.G., Iredale, J.P. (2011). Matrix stiffness modulates proliferation, chemotherapeutic response, and dormancy in hepatocellular carcinoma cells. *Hepatology.* **53**, 1192–1205.

Sharma, S., Goswami, R., Rahaman, S.O. (2019). The TRPV4-TAZ Mechanotransduction Signaling Axis in Matrix Stiffness- and TGF β 1-Induced Epithelial-Mesenchymal Transition. *Cel. Mol. Bioeng.* **12**, 139–152.

Stewart, T.A., Yapa, K.T.D.S., Monteith, G.R. (2015). Altered calcium signaling in cancer cells. *Biochim.* **1848**, 2502–2511.

Syed, S., Karadaghy, A., Zustiak, S. (2015). Simple polyacrylamide-based multiwell stiffness assay for the study of stiffness-dependent cell responses. *JoVE.* **52643**.

Taufalele, P.V., VanderBurgh, J.A., Muñoz, A., Zanutelli, M.R., Reinhart-King, C.A. 2019. Fiber alignment drives changes in architectural and mechanical features in collagen matrices. *PLOS ONE.* **14**, e0216537.

Wullkopf, L., West, A.-K.V., Leijnse, N., Cox, T.R., Madsen, C.D., Oddershede, L.B., Erler, J.T. (2018). Cancer cells' ability to mechanically adjust to extracellular matrix stiffness correlates with their invasive potential. *Mol. Biol. Cell.* **29**, 2378–2385.

Yamamoto, K., Korenaga, R., Kamiya, A., Ando, J. (2000). Fluid Shear Stress Activates Ca^{2+} Influx into Human Endothelial Cells via P2X4 Purinoceptors. *Circ. Res.* **87**, 385–391.

Yankaskas, C.L., Bera, K., Stoletov, K., Serra, S.A., Carrillo-Garcia, J., Tuntithavornwat, S., Mistrionis, P., Lewis, J.D., Valverde, M.A., Konstantopoulos, K. (2021). The fluid shear stress sensor TRPM7 regulates tumor cell intravasation. *Sci Adv.* **7**, eabh3457.

Zhu, H., Zhang, H., Jin, F., Fang, M., Huang, M., Yang, C.S., Chen, T., Fu, L., Pan, Z. (2014). Elevated Orai1 expression mediates tumor promoting intracellular Ca^{2+} oscillations in human esophageal squamous cell carcinoma. *Oncotarget.* **5**, 3455–3471.